Calculating the Peierls energy and Peierls stress from atomistic simulations of screw dislocation dynamics: application to bcc tantalum

Guofeng Wang[1]**, Alejandro Strachan**[2]**, Tahir Çağın and William A Goddard III**[3]

Materials and Process Simulation Center, Beckman Institute (139-74), California Institute of Technology, Pasadena, CA 91125, USA

E-mail: wag@wag.caltech.edu

Abstract

We introduce a novel approach to calculating the Peierls energy barrier (and Peierls stress) based on the analysis of the dislocation migration dynamics, which we apply to $1/2a\langle 111\rangle$ screw dislocations in bcc Ta. To study the migration of screw dislocations we use molecular dynamics with a first principles based embedded-atom method force field for Ta. We first distinguish the atoms belonging to the dislocation core based on their atomic strain energies, defining the dislocation core as the 12 atoms with higher strain energies per Burgers vector. We then apply this definition to the moving dislocations (following the dynamics of a $[1-10]$ dipole of $1/2\langle 111\rangle$ screw dislocations at 0.001 K) and extract their Peierls energy barrier (E_P) and Peierls stress (τ_P). From the dynamics of a dislocation dipole, we determine $E_P = 0.032$ eV (and $\tau_P = 790$ MPa) for twinning shear and $E_P = 0.068$ eV (and $\tau_P = 1430$ MPa) for anti-twinning shear, in good agreement with the results by applying direct shear stresses. This dislocation dynamics method provides insights regarding the dislocation migration process, allowing us to determine the continuous path of dislocation migration. We find that under twinning shear the screw dislocation moves along a path at an angle of only 8.5° with the $[1-10]$ direction while for anti-twinning shear it moves along a path at an angle of 29.5° with the $[1-10]$ direction, documenting the magnitude of the violation of the Schmid Law.

[1] Current address: Materials Sciences Division, Lawrence Berkeley National Laboratory, Berkeley, CA 94720, USA.
[2] Current address: Theoretical Division, Los Alamos National Laboratory, Los Alamos, NM 87545, USA.
[3] Author to whom any correspondence should be addressed.

1. Introduction

A first principles based multi-scale modelling of materials first requires an accurate characterization of the fundamental mechanisms governing materials properties at the atomic level. These properties can then be used in mesoscale or macroscopic simulations to predict the properties of new alloys and composites. Molecular dynamics (MD), using accurate force fields (FF) (potentials) derived from *ab initio* quantum mechanics (QM) data, provides a powerful tool to achieve this challenging goal by enabling the dynamical simulation of millions of atoms. In this paper, we focus on the characterization of dislocation properties in Ta that govern its single crystal plasticity.

In bcc metals, $1/2a\langle 111\rangle$ screw dislocations are believed to control the low temperature plastic deformation because their mobility is lower than that of the edge components [1]. Therefore, it is of great interest to determine their Peierls energy barrier (Peierls stress), which is the activation energy (external stress) required to move a dislocation in an otherwise perfect crystal. It has been established that the dislocation core (which is the nonlinear region a few atomic separations from the dislocation centre) of these screw dislocations is a dominant factor in determining their Peierls energy barrier (or Peierls stress) [2]. The continuum linear elasticity theory succeeds in describing the elastic strain field of dislocations, but it excludes the short-range details of crystal lattices. Hence, the continuum theory is not suitable for investigating the role of dislocation core in the dislocation slip process. Alternatively, first principles based atomistic simulations can provide a good description in the nonlinear dislocation core region as illustrated here for $1/2a\langle 111\rangle$ screw dislocations in bcc tantalum (Ta).

In previous atomistic simulations (e.g. [3–5]), the Peierls stress was determined by increasing the applied shear stress and fully relaxing the simulation cell (containing a dislocation) until the dislocation glides. Although this method gives the necessary information (Peierls stress) about dislocation mobility, it does not provide much information about the Peierls energy barrier and the actual path that dislocations follow. In the following, we propose an alternative approach to obtaining Peierls energy barrier and Peierls stress directly from the analysis of a moving dislocation, which we achieve by simulating a dislocation dipole migration process at extremely low temperature (0.001 K). Our approach is based on an atomistic definition of dislocation core.

One of the non-trivial features of plastic deformation for bcc metals is the observed violation of the Schmid Law (which states that the critical resolved shear stress is constant and independent of the slip system and the external stress) at low temperatures. Duesbery and Vitek [6] pointed out that the twinning and anti-twinning slip asymmetry of shear on {112} planes of the bcc lattice is the intrinsic factor underlying the breakdown in the Schmid Law. Owing to this asymmetry of bcc lattice, the minimal shear stress to make a screw dislocation glide along [111] and [−1−1−1] directions in {112} planes are not equal. Previous experimental and theoretical results of Peierls stresses (see [6] and references therein) have confirmed this point. However, the difference in the path and energetics experienced by the dislocations are unknown although the Peierls stresses for twinning and anti-twinning glides have been calculated. By measuring the dislocation core energy as a continuous function of position in the bcc lattice, we could show the twinning and anti-twinning slip asymmetry of the Peierls energy surface and dislocation trajectories.

As described in section 2, we use an embedded-atom method (EAM) type FF (denoted qEAM) for Ta derived from first principles QM (density functional theory using the generalized gradient approximation). Section 3 reports the studies of the equilibrium dislocation core structure and core energy that we use to propose an atomistic definition of the dislocation core. Section 4 describes our approach for calculating Peierls energy barrier and Peierls stress.

We have applied this approach in a preceding paper [7]. Finally, our conclusions are given in section 5.

2. The qEAM FF

The EAM was first proposed by Daw and Baskes [8, 9] and has been successfully applied to fcc and bcc metals. Our qEAM FF uses a functional form similar to that proposed by Chantasiriwan and Milstein [10]. The total energy of a system with atomic positions $\{r_i\}$ is given by:

$$E = \sum_i F(\rho_i) + \sum_{i<j} \phi(r_{ij}) \tag{1}$$

with

$$\rho_i = \sum_{i \neq j} f(r_{ij}) \tag{2}$$

where $F(\rho)$ is the embedding energy, ρ_i is the total electron density at site i, $f(r_{ij})$ is the electron density function, $\phi(r_{ij})$ is the pair potential function, and r_{ij} is the distance between atoms i and j.

The electronic density is given by

$$f(r) = \frac{[1 + a_1 \cos(\alpha r/V^{1/3}) + a_2 \sin(\alpha r/V^{1/3})]}{r^\beta} \tag{3}$$

where V is the volume per atom, $a_1 = 0.072\,932\,38$, $a_2 = 0.157\,816\,72$, $\alpha(1/\text{Å}) = 21.796\,090\,53$, and $\beta = 7.793\,294\,26$.

The pair potential $\phi(r)$ is taken to be a polynomial function,

$$\phi(r) = (r - r_{\mathrm{m}})^4 [b_0 + b_1 r + b_2 r^2 + b_3 r^3 + b_4 r^4 + b_5 r^5 + b_6 r^6 + b_7 r^7] \tag{4}$$

where $r_{\mathrm{m}}(\text{Å}) = 4.812\,539\,68$ is the cutoff radius. The parameters b_i have the units of eV/Å$^{(4+i)}$ with $b_0 = 6.502\,815\,87$, $b_1 = -11.264\,551\,30$, $b_2 = 8.014\,515\,44$, $b_3 = -2.972\,992\,23$, $b_4 = 0.600\,042\,06$, $b_5 = -0.062\,221\,06$, $b_6 = 0.002\,588\,01$, and $b_7 = -0.000\,005\,04$.

The embedding function $F(\rho)$ is determined from the Rose universal equation of state [11],

$$F(\rho) = E_{\mathrm{EOS}}(a^*) - \frac{1}{2} \sum \phi(r) \tag{5a}$$

where

$$E_{\mathrm{EOS}}(a^*) = -E_{\mathrm{coh}}(1 + a^* + ka^{*3} + f_4 a^{*4})\, \mathrm{e}^{-a^*} \tag{5b}$$

with

$$a^* = \frac{a - a_0}{a_0 \lambda} \tag{5c}$$

The parameters entering the definition of the embedding energy are: $a_0(\text{Å}) = 3.323\,892\,19$, $E_{\mathrm{coh}}(\mathrm{eV}) = 8.154\,204$, $\lambda = 0.207\,828$, $k = -0.007\,178\,01$, and $f_4 = -0.000\,005\,04$.

Our qEAM FF was parameterized to reproduce a set of *ab initio* data for Ta that includes: (a) zero temperature energy and pressure as a function of volume (including large compressions and expansions) for the bcc, fcc, and A15 phases; (b) elastic constants; (c) vacancy and surface formation energies; (d) energetics of a shear deformation in the twinning direction that takes the bcc crystal back to itself. Reference [12] gives the details of the FF optimization procedure.
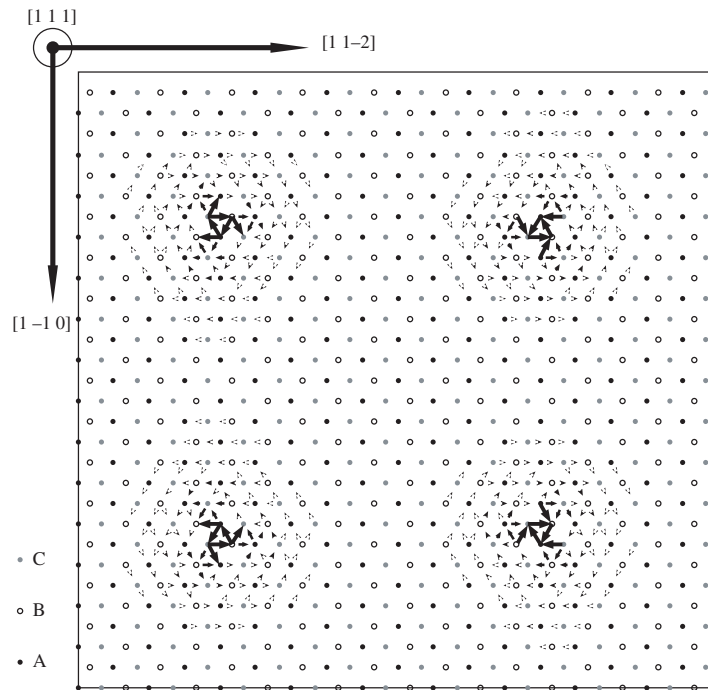
Figure 1. DD map for the equilibrium dislocation quadrupole, in which there are 5670 atoms and each dislocation is 7 *b* long.

3. Atomistic definition of screw dislocation core

3.1. Dislocation core structure

In order to obtain an atomistic description of the equilibrium dislocation structures, we used a periodic simulation cell containing four dislocations (two of the dislocations have Burgers vector $\boldsymbol{b} = a/2[111]$ and the other two have $\boldsymbol{b} = a/2[-1-1-1]$) in a quadrupolar arrangement. The quadruple arrangement (as opposed to a dipole) leads to no positional misfit of atoms across the cell boundary due to the effect of periodic images. The dislocations are located at the geometric centres of a triangle surrounded with three [111] columns of atoms. After building the dislocations using atomic displacements obtained from elasticity theory, we minimized the energy of system with respect to atomic coordinates. For the bcc structure, there are two kinds of dislocation core configurations that can be transformed to each other by reversing the Burgers vector; they are called 'easy core' and 'hard core' [13]. The easy core is the lower energy form and the only one we find from energy minimization. Indeed, our dynamical simulations (section 4.1) show that the dislocation moves from one easy form to an adjacent one avoiding the high-energy hard core. Therefore, we focus our study only on the easy core dislocations.

Figure 1 shows the differential displacement (DD) map for a dislocation quadruple after relaxing the atomic positions using the qEAM FF. In this map, the atoms are represented by circles and projected on a (111) plane of the bcc lattice. The arrows indicate the relative displacements of neighbouring atoms in the [111] direction with respect to their positions in the perfect bcc crystal. The direction of the arrow represents the sign of the displacement and the

magnitude of the arrow is proportional to the relative displacement between the corresponding atoms. When an arrow spans the full distance between two atoms, the relative displacement is $b/3$. As seen from the DD map, the equilibrium dislocation cores (predicted using the qEAM) spread out in three $\langle 112 \rangle$ directions on $\{110\}$ planes. This type of dislocation core is called 'asymmetric core', which breaks the two-fold rotation symmetries (C_2) around the three $\langle 110 \rangle$ directions perpendicular to the dislocation axis. In contrast to our result, a 'symmetric core' is the dislocation core has full D_3 symmetry. Previous atomistic simulations for bcc metals have led to both asymmetric (e.g. [2, 6, 13]) and symmetric (e.g. [6, 14, 15]) core structures for $a/2\langle 111 \rangle$ screw dislocations. In a recent work [16], we showed that the equilibrium core structure itself does not determine the Peierls stress for screw dislocations. Instead we find that the symmetric core must first change into an asymmetric core before its motion. As a result, our approach presented here is applicable for both symmetric core and asymmetric core screw dislocations. The qEAM FF employed in this work is the qEAM1 potential in [16].

3.2. Atomistic definition of dislocation core

We define the strain energy associated with each atom as in equation (6):

$$E_i = F(\rho_i) + \frac{1}{2} \sum_{j \neq i} \phi(r_{ij}) - E^{\mathrm{coh}} \tag{6}$$

where E^{coh} is the atomic cohesive energy in perfect bcc crystal at zero pressure.

The atomic strain energies calculated using equation (6) for the relaxed dislocation quadruple with 5670 atoms (with cell size: $\mathbf{X} = 9a[11\overline{2}]$, $\mathbf{Y} = 15a[1\overline{1}0]$, and $\mathbf{Z} = 7a/2[111]$) are displayed in figure 2(a). Here each atom is projected on the (111) plane and drawn as a circle whose radius is proportional to its atomic strain energy. Most atoms have very small strain energies with only 12 atoms close to the dislocation line showing significant strain energies. Figure 2(b) shows the atomic strain energy distribution per dislocation per Burgers vector for the same dislocation quadruple cell. We find that the atomic strain energy of the six atoms closer to the dislocation line is 0.15–0.17 eV while another six atoms have atomic strain energies ranging from 0.06 to 0.08 eV. The 12 atoms near the centre of the dislocation in figure 2(a) are denoted as A, B, C, and D in figure 2(b), in the decreasing order of atomic strain energy. Except for these 12 atoms, all other atoms have atomic strain energies less than 0.05 eV. Based on these observations, we define the dislocation core (one Burgers vector long) to be formed by the 12 atoms with higher strain energy. For Ta, this leads to the dislocation core energy of $E_c = 1.400\,\mathrm{eV}\,b^{-1}$ in this work. Our atomistic definition of dislocation core is similar in nature to the approach used by Bulatov *et al* [17] where the atomic bond number is used to distinguish core atoms in the 30° partial dislocation in Si.

Corresponding to our definition of dislocation core, we define the core radius as the average distance from the dislocation centre to the closest non-core atoms encircling the core region. This is shown in figure 3 as the dotted line. This leads to a core radius of $r_c = 2.287b$.

It should be noted that we did not relax the cell parameters in the previous quadrupole simulations but used the perfect crystal values. As a result, the final relaxed simulation cell is under the stress (in the 5670-atom cell we obtained $\sigma_{xx} = 210\,\mathrm{MPa}$, $\sigma_{yy} = 200\,\mathrm{MPa}$, and $\sigma_{zz} = -50\,\mathrm{MPa}$). If we relax the lattice parameters of the simulation cell to zero stress, the screw dislocation core dilates to achieve its stress-free state (the core is still formed by the 12 atoms with higher strain energy). We found that the core energy for this stress-free dislocation is $1.386\,\mathrm{eV}\,b^{-1}$, only 1% lower than $1.400\,\mathrm{eV}\,b^{-1}$ corresponding to the case of unrelaxed simulation cell. Thus, even for a relatively small simulation cell the effect of the remnant stress on dislocation core is minor.
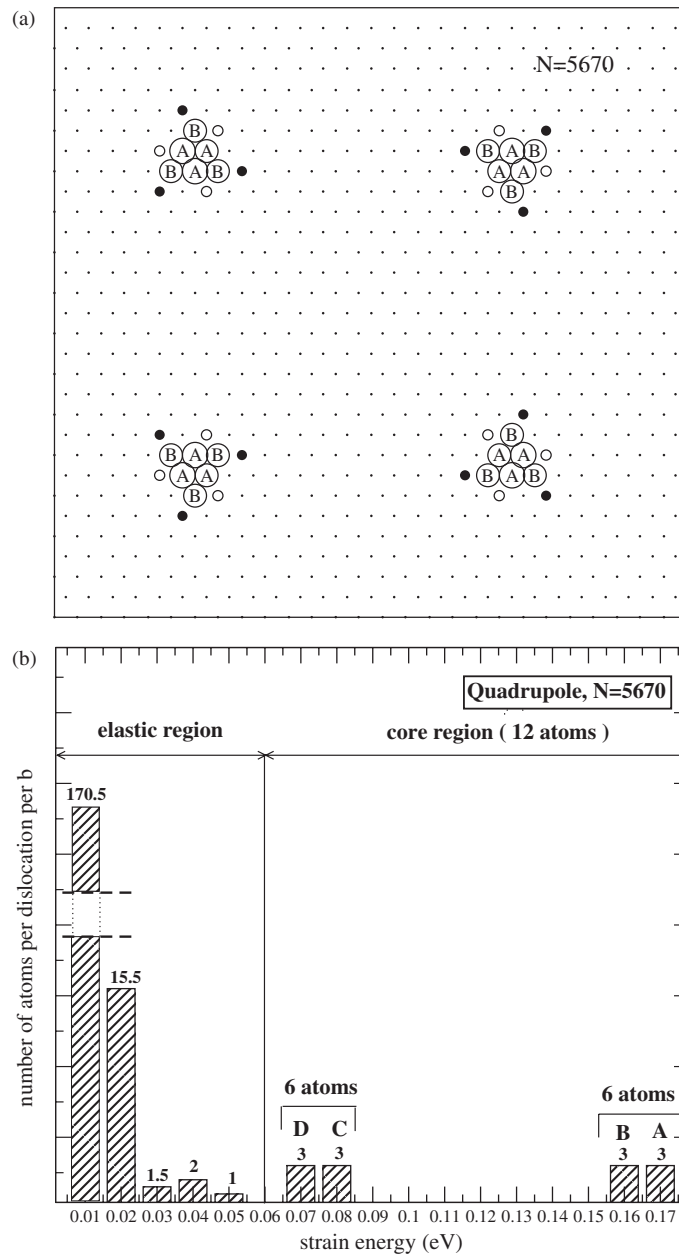
Figure 2. (a) The ⟨111⟩ projection of atomic strain energy distribution for a 1 *b* thick slab in an equilibrated dislocation quadrupole in which there are 5670 atoms and each dislocation is 7 *b* long. (b) Histogram of atomic strain energy distribution for a 1 *b* segment of a dislocation obtained from the same quadrupole simulation. The number of atoms in each energy bin is shown on the top of the corresponding bar. In both (a) and (b), we denote as 'A' the atoms with atomic strain energy ranging from 0.165 to 0.170 eV and we denote as 'B' atoms with atomic strain energy ranging from 0.156 to 0.157 eV. Atoms 'C' in (b) are represented as black circles in (a), while atoms 'D' in (b) are represented as white circles in (a). The atoms labelled by 'C' have higher strain energy than the atoms 'D'.
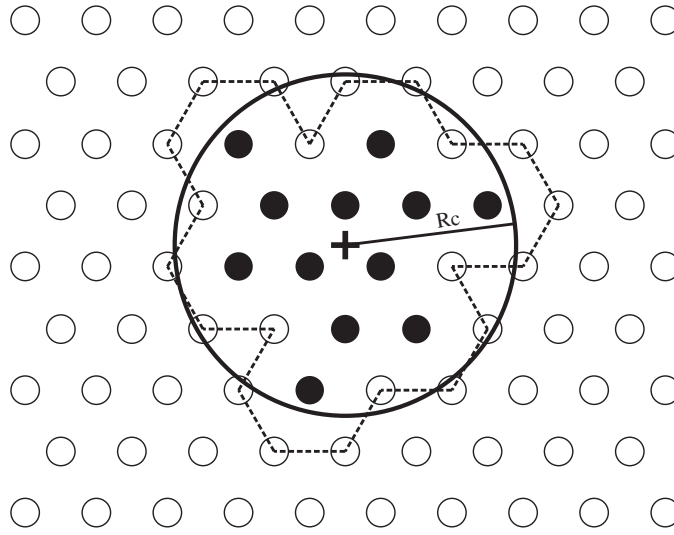
Figure 3. Schematic drawings for a dislocation core in the atomistic model and in the continuum model. Atoms are projected onto the (111) plane and represented by circles. The black circles indicate the atoms constituting the dislocation core according to the atomistic definition, the other atoms are in the elastic region and drawn as white circles. The dotted line connects the non-core atoms that most closely encircle the dislocation core providing a cutoff boundary for the atomistic model. The solid circle whose radius is the average distance from the dislocation centre to the atomistic cutoff boundary (2.287 b) is the dislocation core radius for the continuum model.

3.3. Verification using elasticity theory

In elasticity theory, the total strain energy per Burgers vector for two parallel straight dislocations with equal and opposite Burgers vectors at a separation d is:

$$E = 2E_c(r_c) + 2Kb^3 \ln\left(\frac{d}{r_c}\right) \tag{7}$$

where r_c is the core radius of the dislocation and the elastic modulus K can be expressed as

$$K = \frac{\{S_{11}/[S_{44}(S_{11}S_{44} - S_{15}^2)]\}^{1/2}}{4\pi} \tag{8}$$

Here S_{11}, S_{44}, and S_{15} are modified elastic compliance constants that are determined by the standard elastic constants of the cubic crystal [18].

Summing the pair interactions in equation (7) leads to the total energy per dislocation per Burgers vector in a dislocation quadrupole cell as in equation (9) [14]

$$E = E_c(r_c) + Kb^3 \left[\ln\left(\frac{d_1}{r_c}\right) + A\left(\frac{d_1}{d_2}\right)\right] \tag{9}$$

where d_1 and d_2 are the distances between the dislocations along the [1−10] and [11−2] directions, b is the length of Burgers vector, and $A(d_1/d_2)$ contains all pair-wise interactions and depends on the cell geometry. In order to make the interaction energy summation absolutely convergent, we group the four dislocations in each periodic cell and sum the cell–cell interactions. In equation (9), the core energy $E_c(r_c)$ and effective elastic parameter Kb^3 are constants, leading to a total strain energy that varies linearly with the scaled elastic energy $[\ln(d_1/r_c) + A(d_1/d_2)]$, as the size of simulation cell is changed. Plotting the total strain energy versus the scaled elastic energy, we determine the effective elastic modulus K from the

Table 1. Table of size of simulation cells, number of atoms per simulation cell and strain energy per dislocation per Burgers vector. $X, Y,$ and Z are the cell parameters for the simulation cells. X is in the unit of $a[11\bar{2}]$, Y is in the unit of $a[1\bar{1}0]$, and Z is in the unit of $a/2[111]$. $|X|$, $|Y|$, and $|Z|$ denote the size of simulation cells in unit of Å.

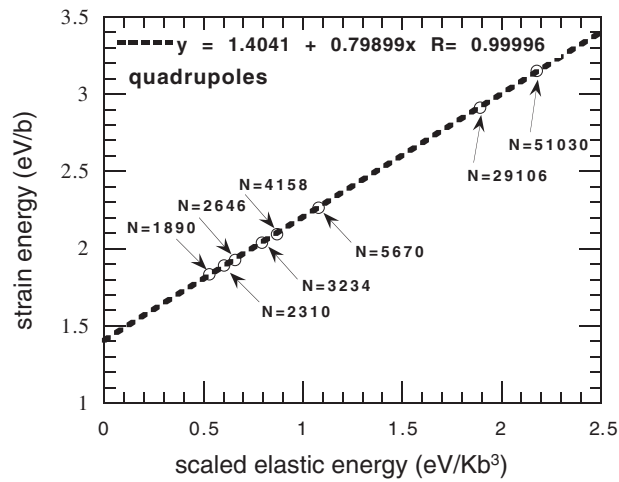|	X	Y	Z	$\lvert X \rvert$ (Å)	$\lvert Y \rvert$ (Å)	$\lvert Z \rvert$ (Å)	N (/cell)	E (eV b^{-1})
1	5	9	7	40.71	42.31	20.15	1 890	1.833
2	5	11	7	40.71	51.71	20.15	2 310	1.891
3	7	9	7	56.99	42.31	20.15	2 646	1.927
4	7	11	7	56.99	51.71	20.15	3 234	2.039
5	9	11	7	73.28	51.71	20.15	4 158	2.095
6	9	15	7	73.28	70.51	20.15	5 670	2.265
7	21	33	7	171.0	155.1	20.15	29 106	2.912
8	27	45	7	219.8	211.5	20.15	51 030	3.150

Figure 4. The strain energy (E/b) as a function of the scaled elastic energy $[\ln(d_1/r_c) + A(d_1/d_2)]$ obtained from the simulations of various dislocation quadruples. The dotted line represents the linear fitting $E/b = 1.4041 + 0.798\,99[\ln(d_1/r_c) + A(d_1/d_2)]$ with $r_c = 2.287\,b$ leading to a dislocation core energy of 1.4041 eV b^{-1}. The number of atoms in each simulation cell is specified in the figure.

slope and the core energy $E_c(r_c)$ from the intercept. The core energy $E_c(r_c)$ obtained in this way depends on the choice of r_c while K does not.

To determine $E_c(r_c)$ and K using equation (9), we simulated quadrupole arrays of dislocations for various system sizes ranging from 1890 atoms (40.71 Å × 42.31 Å × 20.15 Å) to 51 030 atoms (219.8 Å × 211.5 Å × 20.15 Å) and optimized the atomic coordinates by minimizing energy. The geometrical parameters of the simulation cells, numbers of the atoms and the obtained strain energies are shown in table 1. In figure 4, we show the total strain energy for various simulation cells as a function of the scaled elastic energy $[\ln(d_1/r_c) + A(d_1/d_2)]$ which show the linear dependence expected from equation (9).

The linear fit from figure 4 leads to an elastic modulus of $K = 3.3497 \times 10^{-2}$ eV Å^{-3}. Alternatively using the computed elastic constants [12] for the bcc crystal from the qEAM FF, we obtain the $K = 3.3492 \times 10^{-2}$ eV Å^{-3}, which is within 0.02% of the value derived from fitting equation (9) in figure 4. Taking the core radius as $2.287\,b$ obtained from the atomistic definition and using the linear fit of our data in figure 4, we determine the core

Table 2. The lattice parameters and volumes for simulation cells (containing the $[1\bar{1}0]$ dislocation dipole) with zero stress, bulk lattice parameters, and different pure shear stresses. α denotes the angle between Y and Z; β denotes the angle between Z and X; while γ denotes the angle between X and Y.

	$|X|$ (Å)	$|Y|$ (Å)	$|Z|$ (Å)	α	β	γ	Volume (Å^3)
$\sigma_{xz} = 500$ MPa	73.38	70.54	20.13	90.00	91.59	90.00	104 178
$\sigma_{xz} = 300$ MPa	73.37	70.54	20.13	90.00	91.39	90.00	104 172
$\sigma_{xz} = 0$ MPa	73.36	70.55	20.13	90.00	91.12	90.00	104 170
$\sigma_{xz} = -300$ MPa	73.35	70.56	20.13	90.00	90.84	90.00	104 168
$\sigma_{xz} = -500$ MPa	73.34	70.56	20.13	90.00	90.67	90.00	104 167
$\sigma_{xz} = -1100$ MPa	73.34	70.57	20.13	90.00	90.13	90.00	104 174
Bulk lattice parameter	73.27	70.51	20.15	90.00	90.00	90.00	104 110

energy of $1.404\,\text{eV}\,b^{-1}$ for $1/2a\langle111\rangle$ screw dislocations. As expected, this result is in excellent agreement with the dislocation core energy of $1.400\,\text{eV}\,b^{-1}$ calculated directly using the atomistic definition.

4. Peierls energy barrier and Peierls stress from screw dislocation dipole migration

4.1. Dislocation dipole migration and annihilation process

We constructed a dislocation dipole in a periodic simulation cell (two dislocations with opposite Burgers vectors) using elasticity theory. The simulation cell contains 5670 atoms with lattice vectors $X = 9a[11-2]$, $Y = 15a[1-10]$, and $Z = 7a/2[111]$. In the simulation cell, the dislocation with $b = a/2[111]$ and $b = a/2[-1-1-1]$ are positioned at $(1/2X, 3/4Y)$ and $(1/2X, 1/4Y)$ in the (111) plane, respectively. This is denoted as the $[1-10]$ dislocation dipole. Keeping the lattice parameters fixed to the perfect crystal values, the introduction of this $[1-10]$ dislocation dipole causes stresses of $\sigma_{xz} = -1080$ MPa, $\sigma_{xx} = 410$ MPa, $\sigma_{yy} = 530$ MPa, $\sigma_{zz} = 250$ MPa, and $\sigma_{xy} = 0$, $\sigma_{yz} = 0$. The large xz shear stress is due to the misfit of atomic positions in the $(1-12)$ cell boundary (see appendix). To eliminate the mismatch on the $(1-12)$ boundary for periodic dislocation dipoles, we relaxed the stress of the infinite (periodic) simulation cell with isobaric, isothermal (NPT ensemble) MD simulations (with the Rahman–Parrinello barostat [19] and the Nose–Hoover thermostat [20]) at zero stress and $T = 0.001$ K. The final lattice parameters are given in line 3 of table 2.

To make dislocations move, we applied an external shear stress to our simulation cell. For the $[1-10]$ dislocation dipole, both dislocations are sheared in the twinning sense under the shear stress along the [111] direction on the $(1-12)$ plane ($\sigma_{xz} > 0$) and in the anti-twinning sense when the shear stress is in the $[-1-1-1]$ direction on the $(1-12)$ plane ($\sigma_{xz} < 0$). In these two cases ($\sigma_{xz} > 0$ and $\sigma_{xz} < 0$), we start from zero stress and then increase (twinning) or decrease (anti-twinning) the applied shear stress σ_{xz} in steps of 100 MPa until the dislocations begin to move. For each stress state, we performed 10 ps of NPT MD simulation followed by 25 ps of NVT MD simulation at 0.001 K with cell parameters set to the average values of the NPT run. Therefore, there is only pure shear stress in our dipole simulation cells. The Peierls energies (and stresses) reported later correspond to stress-free conditions (except applied shear stress). Thus, the effect of non-glide stresses on the computed Peierls energy barrier (or Peierls stress) [21] has been eliminated. Table 2 gives the lattice parameters for different shears. We find that the dislocation dipole starts to move under twinning shear of $\sigma_{xz} = 500$ MPa and anti-twinning shear of $\sigma_{xz} = -1100$ MPa.
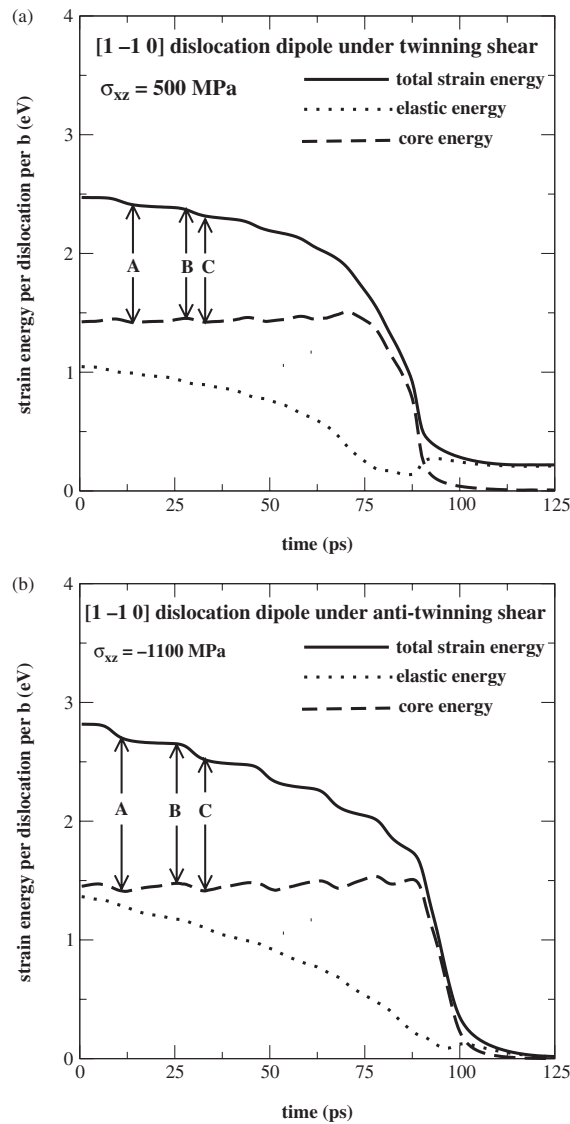
Figure 5. The variation of the total strain energy, elastic energy, and core energy with time in the NVT MD simulations at $T = 0.001$ K. These simulations describe the migration and annihilation of the $[1-10]$ dislocation dipole under the smallest shear stress required for dislocation migration. (*a*) Twinning shear ($\sigma_{xz} = 500$ MPa) and (*b*) anti-twinning shear ($\sigma_{xz} = -1100$ MPa). There are 5670 atoms in the periodic simulation cell. The states A and C correspond to the minimum core energy configurations while state B corresponds to the maximum core energy configuration as shown in figure 7. The detailed structures for these states are shown in figure 6 using the corresponding DD maps.

Once the dislocation dipole starts to move under the applied shear stress, we continued the NVT MD simulation up to 125 ps. In the course of the simulation, the dislocations move continuously until they meet and annihilate. The solid lines in figures 5(*a*) (twinning) and (*b*) (anti-twinning) show the time evolution of the total strain energy (the sum of the atomic strain energies calculated using equation (6)) per dislocation per Burgers vector during
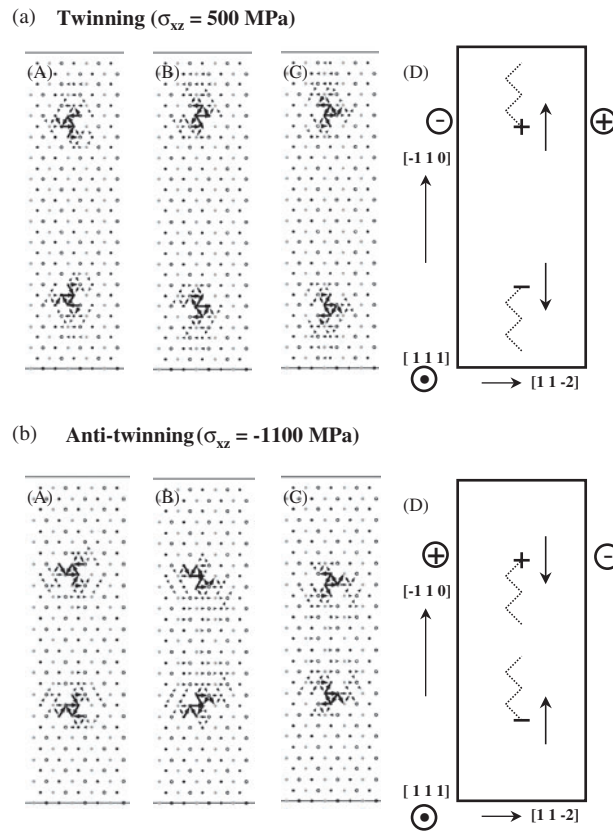
(a)   **Twinning (σ_{xz} = 500 MPa)**

(b)   **Anti-twinning (σ_{xz} = -1100 MPa)**

Figure 6. DD maps showing several snapshots of the dynamical process of dislocation migration and annihilation under (*a*) twinning and (*b*) anti-twinning shear. Panels (A) and (C) show the equilibrated dislocation dipoles while (B) shows the dislocation dipoles at halfway positions between two equilibrium states. These maps show only the central region of the simulation cell containing 5670 atoms. Panels (D) shows [111] projections of dislocation dipole. The dotted line in (D) plots the dislocation slip, which shows to zigzag along ⟨112⟩ directions in {110} planes. The arrow beside the dislocations (drawn as plus sign and minus sign) in panel (D) indicates the direction of the Peach–Koehler force for that dislocation introduced by the applied shear stress. The directions of the shear stresses σ_{xz} are represented by the plus sign ([111]) and minus sign ([−1−1−1]) in the circles in panel (D).

the dislocation migration and annihilation process. The total strain energy decreases as the dislocations approach each other. The rapid drop of the total strain energy at the end indicates dislocation annihilation. Figure 5(*a*) for the twinning shear ($\sigma_{xz} = 500$ MPa) shows a residual total strain energy of 0.2 eV (per dislocation per Burgers vector) after dislocation annihilation. This is because the cell parameters of the dislocation dipole under this shear are different from the cell parameters for the perfect bcc Ta crystal (see, table 2). However, there is little residual strain energy in figure 5(*b*) for the anti-twinning shear ($\sigma_{xz} = -1100$ MPa), because the lattice parameters of the simulation cell under $\sigma_{xz} = -1100$ MPa are very close to those of perfect crystal (as shown in table 2).

Figure 5 shows that the total strain energies exhibit bumps on top of the generally monotonic decrease as the dislocations migrate. To understand the origin of these bumps, figure 6 shows the DD maps of the dislocation dipole for the points labelled as A, B, and C

in figure 5. Panels (A) and (C) in figures 6(*a*) and 6(*b*) show that the valleys of the energy bumps have configurations in which the dislocations are in equilibrium positions. In contrast, panel (B) shows that the peak of the energy bump corresponds to the configuration in which the dislocation is halfway between two equilibrium positions. Thus, the bumps in total strain energy relate to the dislocation motion through a periodic Peierls energy barrier of lattice resistance. Figure 6 (DD maps) also shows that during each step the dislocation moves by $a/3\langle 112\rangle$ on $\{110\}$ planes regardless of the sense (twinning or anti-twinning) of shear. This leads to a zigzag path for dislocation motion as shown by the dotted lines in panel (D).

In section 3.2, we defined the dislocation core (one Burger vector long) as the 12 atoms with higher strain energy for an equilibrium screw dislocation. We now apply this definition to every configuration of our system during its evolution. In this way, the total strain energy of our system can be partitioned into two parts: core energy and elastic energy. The dashed lines in figure 5 show the time evolution of the core energy and the dotted lines show the similar curve for the elastic energy. The core energy is rather constant throughout the dislocation migration process, showing bumps at the same places as the total strain energy. The core energy drops rapidly to zero as the dislocation pair annihilates. In contrast, the elastic energy decreases smoothly (with no bumps) and monotonically as the two dislocations move towards each other.

4.2. Peierls energy barrier and Peierls stress

We define the dislocation position as the strain-energy weighted geometric centre of the 12 atoms forming the dislocation core. Figure 7(*a*) shows the variation of dislocation core energy as a function of distance travelled by the dislocation for the case of twinning shear and figure 7(*b*) shows the same quantity for the case of anti-twinning shear. Both core energy variation curves fit well the following cosine function:

$$E_c(x) = \frac{E_P}{2}\left[1 - \cos\left(\frac{2\pi x}{L} + \varphi\right)\right] + k \cdot x + E_c \tag{10}$$

Here, x is the distance travelled by the dislocation and $E_c(x)$ is the dislocation core energy at point x. $x = 0$ represents the initial dislocation position at the beginning of our NVT MD simulation. The parameter E_P is the Peierls energy barrier, L is the translation distance for a single dislocation jump, and E_c is the dislocation core energy at its equilibrium position. We introduce the phase shift φ in the equation because the dislocation has already started its motion at $x = 0$ under the shear stress in our NVT MD simulations. We also find that the dislocation core energy gradually and slowly increases during the dislocation translation under shears (twinning and anti-twinning). This may be due to the growing attractive elastic interaction between the dislocations as they approach each other. We use a linear term $k \cdot x$ in the above equation to describe this effect. Table 3 gives the fitting parameters for dislocation motion under twinning and anti-twinning shears. The Peierls energy barriers are determined to be $E_P(\text{twinning}) = 0.032$ and $E_P(\text{anti-twinning}) = 0.068$ eV. The anti-twinning to twinning ratio of the Peierls energy barrier is $E_P(\text{anti-twinning})/E_P(\text{twinning}) = 2.125$.

The stress $\tau(x)$ felt by the dislocation during its motion is the derivative of the core energy with respect to the distance it travelled:

$$\tau(x) = \frac{1}{b^2}\frac{dE_c(x)}{dx} \tag{11}$$

Substituting only the cosine term in equation (10) to equation (11) leads to the Peierls stress (the maximum stress from equation (11)) in equation (12).

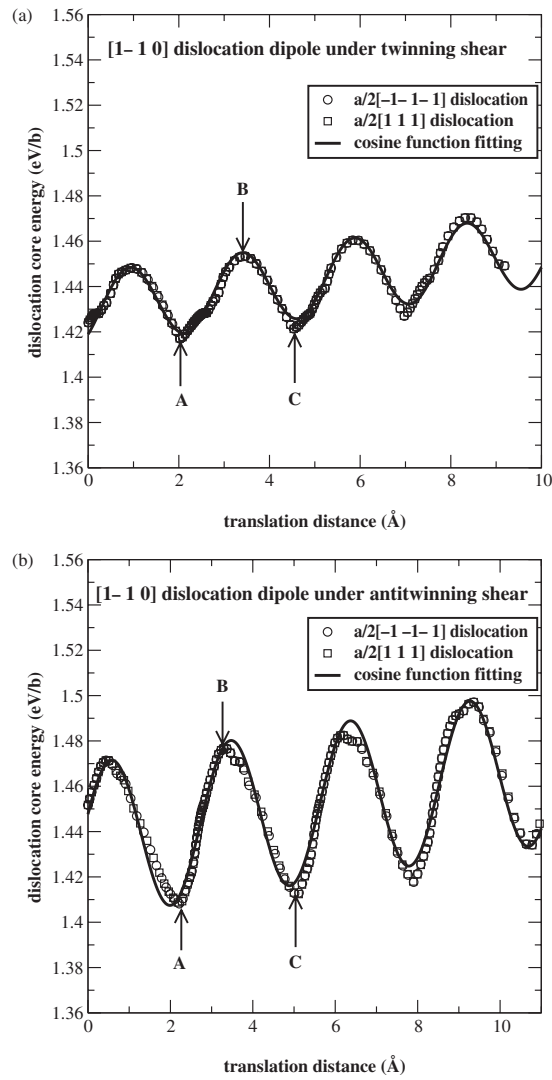$$\tau_P = \frac{1}{b^2}\frac{\pi \cdot E_P}{L} \tag{12}$$

Figure 7. Dislocation core energy as a function of distance travelled by the dislocation under (a) twinning and (b) anti-twinning shear. The solid line shows the cosine plus linear shift function (equation (10)) fit to the atomistic data. Table 3 gives the parameters from optimal fitting. The states, denoted as A, B, and C, correspond to those shown in figure 6.

Using the E_P and L obtained above (table 3) and the Burgers vector $b = 2.88$ Å, we determine Peierls stresses of

$$\tau_P(\text{twinning}) = 790\,\text{MPa} \qquad \text{or} \qquad \frac{\tau_P(\text{twinning})}{\mu} = 0.013$$

$$\tau_P(\text{anti-twinning}) = 1430\,\text{MPa} \qquad \text{or} \qquad \frac{\tau_P(\text{anti-twinning})}{\mu} = 0.024$$

$$\frac{\tau_P(\text{anti-twinning})}{\tau_P(\text{twinning})} = 1.80.$$

Here, the calculated shear modulus for the perfect crystal of $\mu = 62.3\,\text{GPa}$.

Table 3. The parameters obtained from fitting the dislocation (1 b long) core energy to a cosine function (equation (10)) of its translation distance under twinning and anti-twinning shears. The parameters include the Peierls energy barrier E_P in eV, periodic translation distance L in Å, dislocation core energy E_c in eV, phase shift φ, and the slope k of linear term.

	E_P (eV)	L (Å)[a]	$E_c^{[b]}$	φ	k (eV Å^{-1})
Twinning	0.032	2.48	1.414	0.83	0.003
Anti-twinning	0.068	2.90	1.401	1.93	0.003

[a] Compare with $|a/3\langle 112\rangle| = 2.72$ Å in perfect crystal.
[b] Compare with the equilibrium dislocation core energy E_c(eq.) = 1.400 eV.

Table 4. The computed Peierls stresses τ_P in unit of MPa for twinning and anti-twinning shears for $1/2a\langle 111\rangle$ screw dislocation in Ta.

	Ab Inito[a] [3]	$F - S$[b] [4]	MGPT[c] [5]	qEAM (this work)
τ_P (twinning)	670	4120	600	790
τ_P (anti-twinning)	3580	14 800	1380	1430
Anti-twinning–twinning ratio	5.33	3.59	2.29	1.80

[a] The reported τ_P is $0.012G$ for twinning shear and $0.064G$ for anti-twinning shear. The shear modulus G is 56 GPa.
[b] The reported τ_P is $0.05\,C_{44}$ for twinning shear and $0.18\,C_{44}$ for anti-twinning shear. To calculate τ_P in MPa, we used $C_{44} = 82.4$ GPa from [6].
[c] The reported τ_P is $0.0096G$ for twinning shear and $0.022G$ for anti-twinning shear. The shear modulus G is 62.5 GPa.

Using the same qEAM FF and shearing a cylindrical cell containing one dislocation (with periodic boundary conditions in the direction of the Burgers vector), Segall *et al* [22] calculated the Peierls stress to be 740 MPa in good agreement with the 790 MPa derived above for twinning shear. Table 4 compares our results for Peierls stresses with previous calculations using other FFs and *ab initio* method. Our results are reasonably consistent with previous calculations, verifying our approach.

4.3. Twinning and anti-twinning asymmetry

Our results show clearly the twinning and anti-twinning asymmetry of shear for $1/2a\langle 111\rangle$ screw dislocations in bcc Ta. We find an anti-twinning/twinning ratio of 2.125 for Peierls energy barriers and 1.80 for Peierls stresses. Table 3 also shows that the derived dislocation core energy E_c(twinning) = 1.414 eV b^{-1} is 1% higher than E_c(anti-twinning) = 1.401 eV b^{-1}. Both agree quite well with the dislocation core energy E_c(eq.) = 1.400 eV b^{-1} obtained by summing the atomic strain energies for the 12 atoms in the equilibrium dislocation core. The difference between the periodic translation distances for twinning shear (2.48 Å) and anti-twinning shear (2.90 Å) shows that dislocations move differently for these two cases.

Figure 8 shows the trajectories for a dislocation with $\boldsymbol{b} = a/2[-1-1-1]$ (figure 8(a)) (or $\boldsymbol{b} = a/2[111]$ (figure 8(b))) under twinning and anti-twinning shears. The origin of the plot is the initial position for the dislocation. Figure 8 shows that dislocations with $\boldsymbol{b} = a/2[-1-1-1]$ and $\boldsymbol{b} = a/2[111]$ behave similarly under the same sense (twinning or anti-twinning) of shear, while the dislocation moves along completely different trajectories under different senses of shear. Under anti-twinning shear, the dislocation moves along a path at an angle of 29.5° with the $[1-10]$ direction. This angle is close to the 30° for the observed slip system ($\langle 112\rangle$ directions on $\{110\}$ planes) from DD maps. Because the dislocation trajectory is not a straight
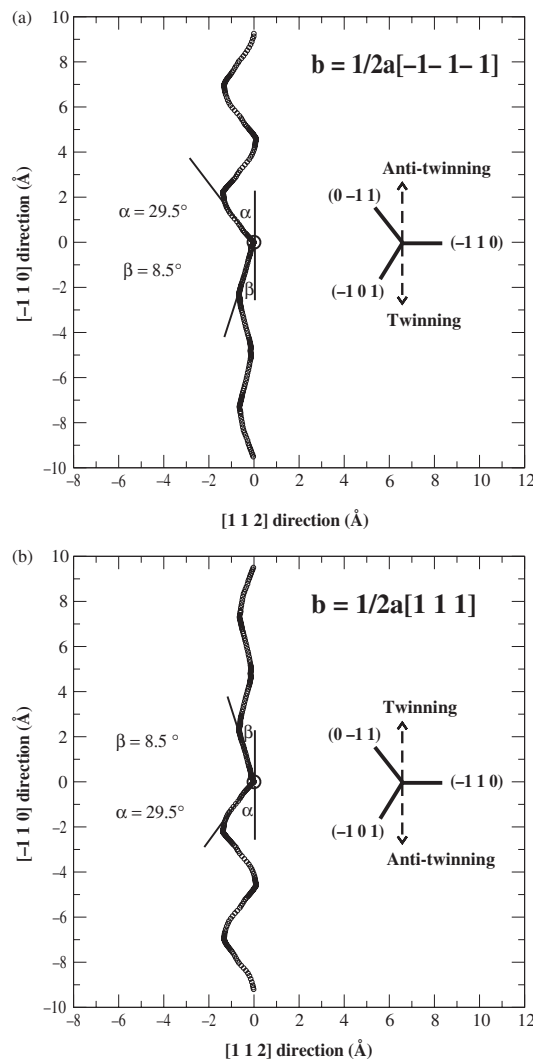
Figure 8. The ⟨111⟩ projection of the trajectory for a moving dislocation with (*a*) *b* = *a*/2[−1−1−1] and (*b*) *b* = *a*/2[111] under twinning and anti-twinning shears. The origin represents the position of the initial equilibrium dislocation. The schematic map on the right shows the crystal geometry and the twinning or anti-twinning direction of shears. The path which dislocation follows under anti-twinning shear makes an angle of *α* = 29.5° with the [1−10] direction while the path which dislocation follows under twinning shear makes an angle of *β* = 8.5° with the [1−10] direction.

line, the periodic translation distance 2.90 Å of this path is larger than $|a/3\langle 112\rangle| = 2.72$ Å. However, the path of the dislocation under twinning shear makes an angle of only 8.5° with the [1−10] direction, leading to a shorter periodic translation distance (2.48 Å).

5. Summary

In this paper, we present the dislocation dynamics approach to calculating Peierls energy barrier and Peierls stress based on an atomistic definition of dislocation core and we apply

it to $1/2a\langle 111 \rangle$ screw dislocations in Ta. Using the first principles based qEAM FF, we calculated the atomic strain energy distribution for equilibrium dislocations. This leads to the conclusion that there are 12 highly strained atoms per dislocation per Burgers vector and these atoms form the dislocation core. Using this definition of dislocation core, we examined the variations of the core energy during dislocation migration. This method gives a Peierls energy barrier of $E_P = 0.032\,\text{eV}$ for twinning shear and $E_P = 0.068\,\text{eV}$ for anti-twinning shear. The predicted Peierls stress is $\tau_P = 790\,\text{MPa}$ for twinning shear and $\tau_P = 1430\,\text{MPa}$ for anti-twinning shear. These values are consistent with those calculated (using the same FF) by shearing a large cylinder containing a single dislocation [22].

We also observe a clear non-Schmid behaviour, which is a consequence of the crystallographic nature of the bcc lattice. The dislocation dynamics method also allow us to follow the continuous path of dislocation migration under dynamics for both twinning and anti-twinning shear. We find that the screw dislocations move in $\langle 112 \rangle$ directions on $\{110\}$ planes both under both twinning and anti-twinning shears, but the actual paths taken by the travelling dislocations differ due to the twinning and anti-twinning asymmetry of the energy landscape. For twinning shear the path of the dislocation makes an angle of only 8.5° with the $[1-10]$ direction, leading to a periodic translation distance of 2.48 Å. However, under anti-twinning shear the dislocation moves along a path at an angle of 29.5° with the $[1-10]$ direction. This angle is close to the 30° for the observed slip system ($\langle 112 \rangle$ directions on $\{110\}$ planes). The periodic translation distance 2.90 Å of this path is only slightly larger than $|a/3\langle 112 \rangle| = 2.72\,\text{Å}$.

Further developments and applications of our approach should quantitatively reveal additional inherent relationships of the Peierls energy barrier and Peierls stress to the structural transformations that the dislocation core undergoes during dynamics.

In this paper, we predict dislocation properties in tantalum from first principles (using no empirical data), an important step in multi-scale modelling of materials. These properties are critical to characterize the mechanical properties of metals at the macroscopic level [23].

Acknowledgments

Appendix

We construct the periodic cells containing a dipole of screw dislocations by starting from a perfect periodic crystal and applying isotropic elasticity theory. This causes a partial stacking fault along the two boundary surfaces of the simulation cell unless the lattice parameters for the simulation cell are also optimized. Thus, to obtain a reference zero-stress simulation cell with no mismatch, we first optimized the simulation cell containing a screw dislocation dipole using NPT MD as described in section 4.1. Otherwise, our simulation cell with 5670 atoms would have a large initial shear stress $\sigma_{xz} = -1080\,\text{MPa}$ and partial stacking faults on $(1-12)$ boundaries, i.e. the two *X*-planes of our simulation cell. As we will show later, the extent of initial mismatch observed upon introduction of a screw dislocation dipole into a perfect crystal model simulation cell is dependent on a geometric factor, the ratio of magnitudes of the simulation cell lengths perpendicular to the dislocation lines, rather than the size of the system.
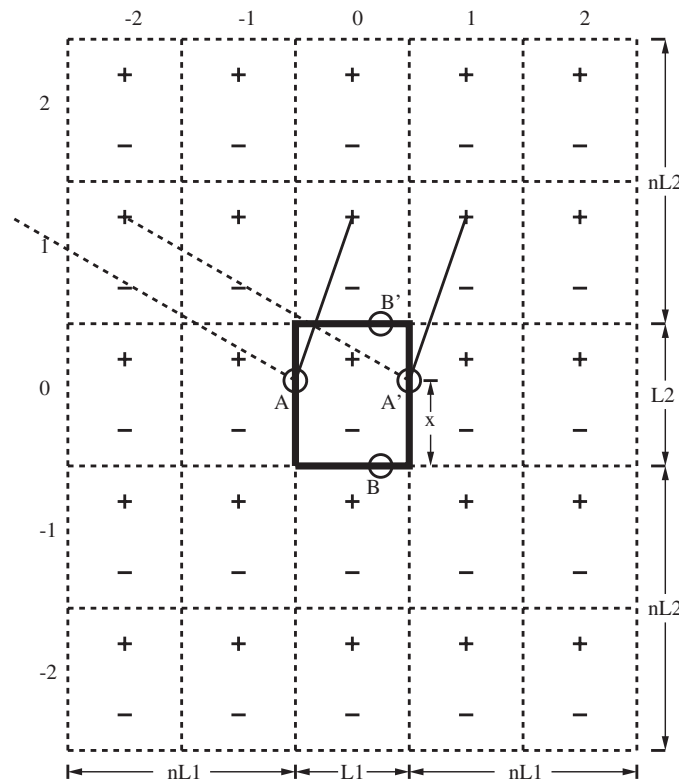
Figure A1. The two-dimensional schematic map of an atomistic simulation cell (solid primary rectangle cell) containing a screw dislocation dipole and its n ($n = 2$) layers of image cells. The lattice parameters of the simulation cell are L_1 and L_2. The Burger vectors of the screw dislocation are normal to the plane. In the cells, the dislocation with Burgers vector $\boldsymbol{b}$ (represented by a plus sign) is at the fractional coordinate $(\frac{1}{2}, \frac{3}{4})$ but the dislocation with Burgers vector $-\boldsymbol{b}$ (represented by a minus sign) is at the fractional coordinates $(\frac{1}{2}, \frac{1}{4})$. The atom A and A′ are on the boundaries parallel to the dislocation dipole and equivalent in the periodic perfect crystal. While the atom B and B′ are on the boundaries perpendicular to the dislocation dipole and also equivalent in the perfect crystal.

Figure A1 shows the scheme we used to compute the atomic displacements for a periodic screw dislocation dipole from isotropic elasticity theory. The rectangular primary dipole cell (in the centre of figure A1) is surrounded with n layers of its periodic image cells. The Burgers vectors of the screw dislocations in the dipole are normal to the plane, leading to atomic displacements only along the direction normal to the plane. Each cell contains a dislocation dipole, where the dislocation with positive (pointing up) Burgers vector has fractional coordinates of $(\frac{1}{2}, \frac{3}{4})$ and the dislocation with negative (pointing down) Burgers vector is at $(\frac{1}{2}, \frac{1}{4})$. The displacements for the atoms in the primary cell are calculated by summing the contributions from all dislocations in the supercell, which includes the primary cell and image cells. The calculated atomic displacements approach their converged values as the number of image cells increases.

We consider next the issue of periodic boundaries in the calculations. Consider two cases:

- Equivalent atoms A and A′ on the boundaries parallel to the dislocation dipole in the crystal cell before the introduction of the screw dislocation dipole.

● Equivalent atoms B and B′ are on the boundaries perpendicular to the dislocation dipole.

We now evaluate the displacement difference between these pairs of atoms caused by the periodic screw dislocation dipoles.

Figure A1 shows that the displacement of the atom A caused by the positive dislocation in the image cell $(1, 0)$ is same as the displacement of the atom A′ caused by the dislocation with the same Burgers vector in the image cell $(1, 1)$. This is because the lines (solid) connecting the atoms to the dislocations are parallel. However, there is no dislocation in the supercell that causes the same amount of displacement to the atom A as the dislocation in the leftmost column of the image cells displaces the atom A′ (as indicated by the dashed lines). Thus, the displacement difference between the atom A and A′ is the displacement of the atom A caused by the dislocations in the rightmost image cells less the displacement of the atom A′ caused by the dislocations in the leftmost column of the image cells, as given in equation (A1).

$$
\Delta d_{\text{A–A}'} = \frac{b}{\pi} \left(\sum_{i=0}^{n} \left\{ \tan^{-1} \left[\frac{(i + (3/4))L_2 - x}{(n + (1/2))L_1} \right] - \tan^{-1} \left[\frac{(i + (1/4))L_2 - x}{(n + (1/2))L_1} \right] \right\} \right.
$$
$$
\left. + \sum_{i=0}^{n-1} \left\{ \tan^{-1} \left[\frac{(i + (3/4))L_2 + x}{(n + (1/2))L_1} \right] - \tan^{-1} \left[\frac{(i + (1/4))L_2 + x}{(n + (1/2))L_1} \right] \right\} \right) \tag{A1}
$$

Here, L_1 and L_2 are the lattice parameters of the primary cell, x is the distance from the atom A (or A′) to the bottom of the primary cell, and n is the number of layers of the image cells.

A similar procedure leads to the displacement between atoms B and B′ given in equation (A2).

$$
\Delta d_{\text{B–B}'} = \frac{b}{\pi} \left(\sum_{i=0}^{n} \left\{ \tan^{-1} \left[\frac{(i + (1/2))L_1 - x}{(n + (1/4))L_2} \right] - \tan^{-1} \left[\frac{(i + (1/2))L_1 - x}{(n + (3/4))L_2} \right] \right\} \right.
$$
$$
\left. + \sum_{i=0}^{n-1} \left\{ \tan^{-1} \left[\frac{(i + (1/2))L_1 + x}{(n + (3/4))L_2} \right] - \tan^{-1} \left[\frac{(i + (1/2))L_1 + x}{(n + (1/4))L_1} \right] \right\} \right) \tag{A2}
$$

Here, x is the distance from the atom B (or B′) to the left boundary of the primary cell.

As n goes to infinity, we find that

$$
\Delta d_{\text{A–A}'} = \frac{b}{\pi} \tan^{-1} \left[\frac{L_2}{L_1} \right], \qquad \text{for all } x \in [0, L_2] \tag{A3}
$$

$$
\Delta d_{\text{B–B}'} = 0, \qquad \text{for all } x \in [0, L_1] \tag{A4}
$$

Equation (A3) implies that for finite values of L_1 and L_2, introducing the periodic screw dislocation dipole makes atoms A and A′ non-equivalent. As a result, a partial stacking fault along the boundary parallel to the dislocation dipole is formed in the crystal cell with the magnitude of this stacking fault determined by the ratio of simulation cell lengths perpendicular to dislocation lines. The geometric factor, L_2/L_1 determines the magnitude of initial mismatch upon construction. This stacking fault disappears when $L_2 \ll L_1$, which corresponds to dislocation dipole annihilation when L_1 is finite.

On the other hand, equation (A4) shows that the periodic screw dislocation dipoles do not cause a stacking fault along the boundary perpendicular to the dislocation dipole in the simulation cell.

References

[1] Louchet F and Kubin L P 1979 *Phil. Mag.* A **39** 433
[2] Vitek V 1974 *Cryst. Latt. Defects* **5** 1
[3] Woodward C and Rao S I 2002 *Phys. Rev. Lett.* **88** 216402
[4] Ito K and Vitek V 2001 *Phil. Mag.* A **81** 1387
[5] Yang L H, Söderlind P and Moriarty J A 2001 *Phil. Mag.* A **81** 1355
[6] Duesbery M S and Vitek V 1998 *Acta Mater.* **46** 1481
[7] Wang G, Strachan A, Çağın T and Goddard W A 2001 *Mater. Sci. Eng.* A **309** 133
[8] Daw M S and Baskes M I 1983 *Phys. Rev. Lett.* **50** 646
[9] Daw M S and Baskes M I 1984 *Phys. Rev.* B **29** 6443
[10] Chantasiriwan S and Milstein F 1996 *Phys. Rev.* B **53** 14080
[11] Rose J H, Ferrante J and Smith J R 1981 *Phys. Rev. Lett.* **47** 675
[12] Strachan A, Çağın T, Gülseren O, Mukherjee S, Cohen R E and Goddard W A 2004 First principles force field
       for metallic Tantalum *Mod. Sim. Mater. Sci. Eng.* **12**
[13] Xu W and Moriarty J A 1996 *Phys. Rev.* B **54** 6941
[14] Ismail-Beigi S and Arias T A 2000 *Phys. Rev. Lett.* **84** 1499
[15] Woodward C and Rao S I 2001 *Phil. Mag.* A **81** 1305
[16] Wang G, Strachan A, Çağın T and Goddard W A 2003 *Phys. Rev.* B **67** 140101(R)
[17] Bulatov V V, Yip S and Argon A S 1995 *Phil. Mag.* A **72** 453
[18] Hirth J P and Lothe J 1982 *Theory of Dislocations* (New York: Wiley)
[19] Parrinello M and Rahman A 1981 *J. Appl. Phys.* **52** 7182
[20] Hoover W G 1985 *Phys. Rev.* A **31** 1695
[21] Duesbery M S 1984 *Proc. R. Soc. Lond.* A **392** 175
[22] Segall D E, Arias T A, Strachan A and Goddard W A 2001 *J. Comput.—Aided Mater. Des.* **8** 161
[23] Cuitiño A M, Stainier L, Wang G, Strachan A, Çağın T, Goddard W A and Ortiz M 2001 *J. Comput.—Aided
       Mater. Des.* **8** 127